IEEE Transactions on Robotics (T-RO) paper, presented at ICRA 2026, Vienna, Austria. Cite as T-RO paper.

Fourigami: A 4-Degree-of-Freedom, Force-Controlled, Origami, Finger Pad Haptic Device

Crystal E. Winston*, Hojung Choi, Rianna Jitosho, Zhenishbek Zhakypov, Jasmin E. Palmer, Mark R. Cutkosky, and Allison M. Okamura

***Abstract*—Skin deformation haptic devices worn on the finger pad provide realistic touch feedback during interactions with virtual objects. Two primary challenges in creating such devices are: (1) making a multi-degree-of-freedom device that is small and lightweight so it does not encumber the wearer and (2) providing accurate control of forces displayed to the finger pad. This work presents a 4-degree-of-freedom (DoF) finger pad haptic device, called Fourigami, that addresses these challenges. We address the first challenge using origami manufacturing methods and pneumatic actuation to fabricate a 25 g prototype that displays normal, shear, and twist and can be easily worn on the finger pad. We address the second challenge using a low-profile, 6-DoF, force/torque sensor to control forces displayed to the finger. Fourigami has a bandwidth ranging from 2-4 Hz depending on direction, and when acting on a human finger, it exerts forces ranging from ± 1.0 N in shear, 4.2 N in normal, and ± 4.2 N·mm of twist. Finally, we demonstrate the device's efficacy when rendering haptic feedback to a user tracking a sinusoidal trajectory and a trajectory representing interactions with a virtual object.**

***Index Terms*—Haptics and Haptic Interfaces, Force Control, Parallel Robots, Soft Robot Materials and Design.**

I. Introduction

Wearable haptic devices have gained acceptance as an alternative to traditional grounded haptic devices for teleoperation, virtual reality (VR), and augmented reality (AR) applications [1]–[3]. They provide a much larger workspace than grounded devices and are less encumbering than heavy exoskeletal systems. By providing deformations to the glabrous (non-hairy) skin of the human finger pads, wearable devices can allow people to perceive contacts and distinguish between objects of different virtual mass or stiffness with results comparable to those obtained with grounded devices [2], [4].

This paper addresses two challenges associated with finger-worn devices. The first is to simulate contacts with normal force, shear force, and torsion in a device that is lightweight and compact enough to be worn on the fingertips. The second is to provide direct control of interaction forces so that consistent forces can be applied across users with finger pads of different dimensions and stiffnesses. We have not been able to address these challenges in our prior work. We have built 4 DoF devices capable of rendering normal force, shear force, and torsion, but they were either relatively heavy and encumbering while not producing compellingly large forces [5] or were capable of rendering large forces in a compact form-factor, but at the expense of closed loop control [6]. Additionally, neither of these devices utilized force control, which is what allows us to compensate for differences in finger pad stiffness and dimensions across users. To the authors' knowledge, Fourigami is also the first wearable device to use closed-loop force control for rendering forces to the finger pad.

In the following sections, we review related work and explain the design, manufacturing process, and characterization

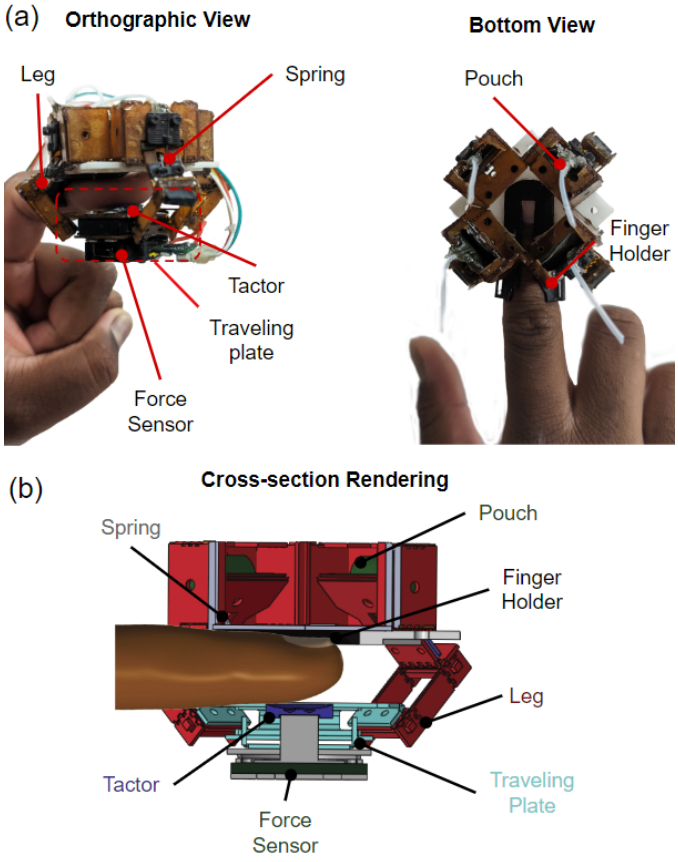

Fig. 1. **(a)** Fourigami device with key components labeled. **(b)** A cross-section CAD rendering illustrating how Fourigami fits on a finger.

*crystalewinston@alumni.stanford.edu

All the authors are with the Department of Mechanical Engineering, Stanford University, CA 94305, USA.

This work was supported by the Stanford Graduate Fellowship, National Science Foundation (NSF) Grant Number 1812966, and the Swiss National Science Foundation (SNSF) Early Postdoc Mobility grant P2ELP2 195132

IEEE Transactions on Robotics (T-RO) paper, presented at ICRA 2026, Vienna, Austria. Cite as T-RO paper.

of *Fourigami*, a novel lightweight, 4 degree-of-freedom (DoF), skin deformation device Fig. 1. Second, we demonstrate direct force control of Fourigami for rendering haptic feedback to the user. Finally, we present results of tests establishing the performance of the device in terms of force output and bandwidth, and also demonstrate it tracking a trajectory that could be realistically generated by interacting with a virtual object. We show that Fourigami is capable of producing a maximum blocked force of ± 2.2 N in the x-axis, ± 2.0 N in the y-axis, 5.6 N in the z-axis, and ± 11 N·mm of torsion, which is on par with or, larger than, similar finger pad haptic devices [2], [5]–[7]. When acting on a finger pad, it applies forces of ± 1.0 N in x- and y-axes, 4.5 N in the z-axis, and ± 4.2 N·mm. The device also has a bandwidth of 2-4 Hz when in contact with a finger phantom, depending on the direction.

II. Prior Work and Our Contributions

To contextualize our work, this section describes several finger pad haptic devices in the literature and highlights the differences and contributions of our development of Fourigami. Researchers have modeled soft, friction-based, contacts with the finger pad as having 4-DoF: two directions that shear the finger pad, one translation that is normal to the finger pad, and one rotation about the vector normal to the finger pad [13], [14]. However, building a wearable device that can provide compelling force feedback with those degrees of freedom that does not encumber the user is a difficult task. This can be observed by comparing the size, mass, and force production capabilities of 2-DoF [8] and 3-DoF [1], [7], [9]–[11] finger pad haptic devices with those that have 4-DoF and higher [5], [12], [15]. This information is summarized in Table I. This is not an exhaustive list, but is a representative set meant to illustrate some of the size, mass, and force production trade-offs that must be made in order to build a multi-DoF device. More comprehensive reviews are provided by Pacchierotti et al. [16] and Adilkhanov et al. [17].

The table shows that the size and mass of these devices tend to increase with the number of degrees of freedom and force production capability. For example, the devices developed by Leonardis et al. [1] and Schorr et al. [2] have the same degrees of freedom and similar actuation strategies. However, the latter is larger and heavier than the former, primarily because it produces nearly 3 N more normal force and comparable shear force. Furthermore, the device developed by Giraud et al. [7] is the lightest 3-DoF device the authors found in the literature. However, the forces that it can produce are, in some directions, an order of magnitude smaller than its other 3-DoF counterparts. Finally, the device developed by Young et al. [12] is capable of producing large forces in 6 DoF, but it has a mass of 610 g, which is more than 10 times the mass of any other device listed in Table I. 2These examples highlight that creating a device that is lightweight, while also having many DoF and producing large forces is a challenge.

To address this, several research groups have turned to origami-inspired design because it enables cheap and scalable fabrication of high DoF structures in a relatively lightweight and compact form factor. For this reason, over the last eight years, there has been a significant increase in the number of origami-inspired haptic devices [18]. Outside of wearable finger pad haptic devices, one of the most notable origami-inspired haptic devices is a portable 3-DoF haptic joystick developed by Mintchev et al. [19]; our device and others [5], [7] use similar fabrication techniques. Within the 4-DoF wearable devices in Table I, all of them are origami inspired.

The primary motivation for developing Fourigami after our prior work from Williams et al. [5] and Zhakypov et al. [6] was to provide a compact device with large force output and closed-loop control. Users noted that the device in [5] was somewhat heavy, thus encumbering their motion, and it did not provide adequate output forces for compelling haptic interaction. The device developed by Giraud et al. [7] is quite similar to Fourigami, but produces relatively small forces. These concerns were addressed by the device developed by Zhakypov et al. [6], but at the expense of closed-loop control, which is vital for VR, AR, and teleoperation applications. Fourigami's relatively large output forces and closed-loop force control differentiate it from other origami-inspired finger pad haptic devices. The primary contributions when compared to our prior work are a lightweight form factor that does not encumber the user along with the addition of closed-loop force control. This allows Fourigami to compensate for variation in finger pad size and stiffness between users.

We directly address the issue of controlling the forces transmitted to the finger pad with force control because it is of particular importance for VR and AR training tasks where accurately displaying object stiffness or mass is important. It is also relevant for haptics studies where a researcher wants to ensure that different users receive the same force feedback and for teleoperation scenarios where users are operating a robot that must handle delicate objects. Previous devices have attempted to do this with position control because integrating a sufficiently small force sensor into the device itself proves challenging [2], [5]. These devices translate force commands into position commands by modeling the finger as a linear spring with known stiffness. However, this approach can cause substantial inaccuracies because the stiffness of the fingers varies dramatically from person to person [20]–[25]. For example, if we look at the finger stiffness data presented by Li et al. [25] showing a sample of 10 individuals interacting with surfaces much stiffer than a human finger, the finger stiffness measurements range from ≈ 0.08 N/mm to ≈ 0.16 N/mm. Furthermore, the relationship between force and displacement for the finger pad is known to be nonlinear [20], [21], [23] meaning that the stiffness of a person's finger cannot be captured by a single value, even though existing position control-based haptic devices rely on this assumption in order to display haptic feedback [2], [5].

Some force-controlled finger pad haptic devices have been developed for similar applications. However, they are either grounded devices that use force sensors too large for wearable devices [26], or they use small single-axis load cells to control tension in tendons 2that drive the device rather than directly controlling forces displayed to the finger pad itself [10]. In both of these cases, extending their presented design strategies to build a wearable 4-DoF device that controls forces displayed

IEEE Transactions on Robotics (T-RO) paper, presented at ICRA 2026, Vienna, Austria. Cite as T-RO paper.

TABLE I
SUMMARY OF DIFFERENT KEY PERFORMANCE AND SIZE METRICS OF A FEW DIFFERENT FINGER PAD HAPTIC DEVICES. †INDICATES AN ITEM THAT WAS NOT LISTED. § INDICATES AN ITEM THAT IS DERIVED BASED ON INFORMATION PROVIDED IN THE PAPER

Reference	Girard et al. [8]	Solazzi et al. [9]	Prattichizzo et al. [10]	Schorr et al. [2]	Leonardis et al. [1]	Giraud et al. [7]	Ma et al. [11]	Williams et al. [5]	Zhakypov and Okamura [6]	*Fourigami* (this paper)	Young et al. [12]
Number of DoF	2	3	3	3	3	3	3	4	4	*4*	6
Normal Blocked Force (N)	N/A	1.97	1.5	7.5	4.16	0.678	7.3	1.4	7	*5.6*	10
Shear Blocked Force (N)	3.4	†	0.75 §	2.0	2.42 - 2.731.3	0.15 - 0.4	7.3	1.1 - 1.6	1.3	*2 - 2.4*	†
Blocked Twisting Torque (Nmm)	N/A	N/A	N/A	N/A	N/A	N/A	N/A	5.6 - 8.2	25	*11 - 13*	†
Bandwidth (Hz)	†	†	10	10	†	†	†	9	6 - 11	*2 - 4*	†
Mass at Fingertip (g)	22	56	30	32	16	13	53.5	50	13.7	*25.2*	610
Dimensions (WXHXD) (mm x mm x mm)	20.4 × 35 × 34.1	†	†	21.5 × 48.8 × 40.2	18 × 32 × 32	36 × 25 × 26	48 × 40 × 79	80 × 80 × 45	†	*54 × 54 × 45*	†
Actuation Method	DC Motors	DC Motors	DC motors	DC Motors	Servos	Piezo-electric Actuators	Pneu-matic	DC Motors	Pneu-matic	*Pneu-matic*	DC motors
Feedback/ Control Method	Position	Position	Tendon Tension	Position	Position	Position	Pressure	Position	Open Loop	*Force*	Position
Origami Inspiration	No	No	No	No	No	Yes	No	Yes	Yes	*Yes*	No

to the finger pad proves challenging because they either do not directly measure forces applied to the finger pad or do so with a force sensor that is too large for wearables. In order to address this challenge, Fourigami uses a lightweight 6-axis force/torque (F/T) sensor that is 21.3 mm in diameter and weighs only 2 g. This F/T sensor is attached to Fourigami's tactor, enabling precise force control.

III. Device Design and Fabrication

A. Device Structure and Components

Fourigami has 4-DoF. It is capable of translating in the x-, y-, and z-axes, and twisting about the z-axis, as illustrated in Fig. 2.

The device is actuated by four pneumatic pouches counteracted by antagonistic springs. These pouches undergo inflation and deflation controlled by four pneumatic pressure regulators (VEAB-B-26-D18-F-V2-1R1, Festo Corp.). These pressure regulators have an output pressure range of -100 to 500 kPa with a nominal flow rate $\geq$ 14.5 L/min and an absolute accuracy of 0.75% FS. Although the regulators have a much larger pressure range, we ensure that the device receives pressures only in the range of -100 kPa to 200 kPa.

Attached to the tactor is a 3D-printed housing that encases a small force sensor used for force-feedback. The tactor is used to apply forces to the finger pad and is covered with a 0.75 mm layer of high-friction silicone (Yreela, Non-slip Silicone Material Roll) to prevent slip between the finger pad and the tactor. Similar high friction rubbers have been used in many other skin deformation-based finger pad haptic devices in order to ensure that the tactor is stretching the skin rather than sliding across it [2], [27], [28]. Although these tactors are made from hyperelastic materials, their nonlinear mechanical properties

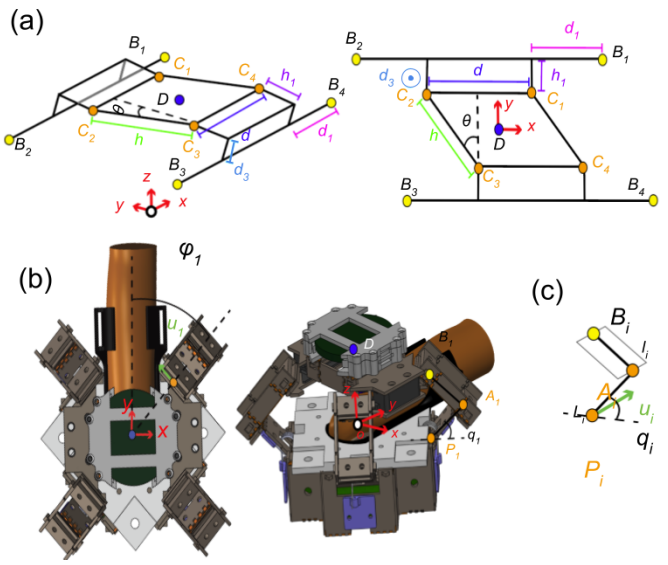

Fig. 2. **(a)** Orthographic and top view of the traveling plate kinematic linkage. **(b)** The Fourigami device with coordinate system and kinematic variables labeled. **(c)** A single leg in plane with kinematic variables.

IEEE Transactions on Robotics (T-RO) paper, presented at ICRA 2026, Vienna, Austria. Cite as T-RO paper.

have not been known to induce noticeable nonlinearities in the system that impede their command tracking accuracy or controllability. Similarly, we observed that the high-friction silicone on Fourigami's tactor did not impede the performance of the device, most likely because it is thin and also quite stiff relative to a human finger pad.

The device is attached to the finger pad with a finger holder. This holder gently clamps to the finger below the distal interphalangeal joint and cups the finger along its back and nail. This attachment method is used to prevent the device from altering the tactile properties of the finger pad while wearing it by ensuring that only the tactor is in direct contact with the finger pad.

The origami structure is made from a fiberglass and polyimide laminate, as described in Section III-D. Within this structure, gaps in the fiberglass expose sections of polyimide, which act as flexible hinges facilitating the origami mechanism's movement.

The traveling plate, which houses the force sensor and enables the twisting degree of freedom, connects the tactor to the device's legs. The traveling plate also has a 3D-printed spacer which determines the neutral height of the tactor. It is also interchangeable, allowing adjustment based on the user's finger size. The device, excluding the tubing, weighs 25.2 g. A set of images labeling these critical components is shown in Fig. 1.

Control of the entire system is managed by a Raspberry Pi 4B (Raspbery Pi Ltd., United Kingdom). This single-board computer reads data from the force sensor, computes the control signals, and sends commands to the pneumatic pressure regulators.

B. Kinematics and Jacobian

Fourigami uses a 4-DoF parallel mechanism containing four legs and a traveling plate. In this section, we describe the kinematics of this mechanism and the device Jacobian, which relates joint velocities to end-effector, or tactor, velocities. The device's structure is inspired by, and very similar to, the 4-DoF manipulators developed by Pierrot et al. [29] and Williams et al.[5].

The point D represents the center of the traveling plate, and is the point that the tactor is attached to. The vector $\overrightarrow{OD} = [x, y, z]^T$ represents the position of the tactor in task space. Due to the symmetry of the device, each of the four legs, $i = 1, 2, 3, 4$, has the same geometric representation and can be analyzed independently. Each of the leg's four joint angles is defined as q_i which rotate about the vector $\overrightarrow{u_i}$ which originates at the point P_i. A_i, B_i, and C_i are the centers of their respective joints, as depicted in Fig. 2. Between A_i and B_i, there is a 4-bar linkage which constrains the traveling plate to only travel in a plane orthogonal to the z axis.

We rename the vector $\overrightarrow{A_iB_i}$ as $\overrightarrow{b_i}$ and observe that the magnitude of the vector $\overrightarrow{b_i}$ is determined by the dimensions of this 4-bar such that

$$\|\overrightarrow{b_i}\| = l_i^2, \tag{1}$$

We also rename the vector $\overrightarrow{P_iA_i}$ as $\overrightarrow{a_i}$. By looking at the device's structure, we also observe that, for each leg,

$$\overrightarrow{OP_i} + \overrightarrow{a_i} + \overrightarrow{b_i} = \overrightarrow{OD} + \overrightarrow{DB_i}, \tag{2}$$

where the vector $\overrightarrow{a_i}$ is defined as

$$\overrightarrow{a_i} = \begin{bmatrix} L\cos\phi_i\cos q_i \\ L\sin\phi_i\cos q_i \\ -L\sin q_i \end{bmatrix} \tag{3}$$

and $\phi_i = \frac{(2i-1)\pi}{4}$.

The vectors $\overrightarrow{DB_i}$ are

$$\begin{aligned} \overrightarrow{DB_1} &= \begin{bmatrix} -\frac{1}{2}h\sin\theta + d_1 + \frac{d}{2} \\ \frac{1}{2}h\cos\theta + h_1 \\ d_3 \end{bmatrix} \\ \overrightarrow{DB_2} &= \begin{bmatrix} -\frac{1}{2}h\sin\theta - d_1 - \frac{d}{2} \\ \frac{1}{2}h\cos\theta + h_1 \\ d_3 \end{bmatrix} \\ \overrightarrow{DB_3} &= \begin{bmatrix} \frac{1}{2}h\sin\theta - d_1 - \frac{d}{2} \\ -\frac{1}{2}h\cos\theta - h_1 \\ d_3 \end{bmatrix} \\ \overrightarrow{DB_4} &= \begin{bmatrix} \frac{1}{2}h\sin\theta + d_1 + \frac{d}{2} \\ -\frac{1}{2}h\cos\theta - h_1 \\ d_3 \end{bmatrix}. \end{aligned} \tag{4}$$

As originally presented in [29], Eq.(1) can be written as a system of four equations

$$I_i\sin q_i + J_i\cos q_i + K_i = 0,$$

where I_i, J_i, and K_i are functions of the device's geometry derived from substituting Eq.(4) and Eq.(3) into Eq.(1). From there, the inverse kinematic solution can be found from the following equation:

$$q_i = 2\,\mathrm{atan2}\left(-I_i \pm \sqrt{\Delta},\, K_i - J_i\right)$$

where $\Delta = \sqrt{I_i^2 - K_i^2 + J_i^2}$.

Taking the time derivative of Eq.(2) gives us:

$$\dot{\overrightarrow{a_i}} + \dot{\overrightarrow{b_i}} = \dot{\overrightarrow{OD}} + \dot{\overrightarrow{DB_i}}, \tag{5}$$

which allows us to derive the jacobian. Noting that $\dot{\overrightarrow{a_i}} = \dot{q_i}\overrightarrow{u_i} \times \overrightarrow{a_i}$ and taking the dot product of both sides of Eq.(5) with $\overrightarrow{d_i}$ allows us to write:

$$J_q\,\dot{\overrightarrow{q}} = J_v\,\overrightarrow{v}$$

where $\overrightarrow{v} = [\dot{x},\, \dot{y},\, \dot{z},\, \dot{\theta}]^T$,

$$J_q = \mathrm{diag}\left(\begin{bmatrix} (\overrightarrow{b_1}\times\overrightarrow{a_1})\cdot\overrightarrow{u_1} \\ (\overrightarrow{b_2}\times\overrightarrow{a_2})\cdot\overrightarrow{u_2} \\ (\overrightarrow{b_3}\times\overrightarrow{a_3})\cdot\overrightarrow{u_3} \\ (\overrightarrow{b_4}\times\overrightarrow{a_4})\cdot\overrightarrow{u_4} \end{bmatrix}\right), \tag{6}$$

and

$$J_v = \begin{bmatrix} \overrightarrow{b_1}^T & -1/2b_{1,x}h\cos\theta - 1/2b_{1,y}h\sin\theta \\ \overrightarrow{b_2}^T & -1/2b_{2,x}h\cos\theta - 1/2b_{2,y}h\sin\theta \\ \overrightarrow{b_3}^T & 1/2b_{3,x}h\cos\theta + 1/2b_{3,y}h\sin\theta \\ \overrightarrow{b_4}^T & 1/2b_{4,x}h\cos\theta + 1/2b_{4,y}h\sin\theta \end{bmatrix} \tag{7}$$

IEEE Transactions on Robotics (T-RO) paper, presented at ICRA 2026, Vienna, Austria. Cite as T-RO paper.

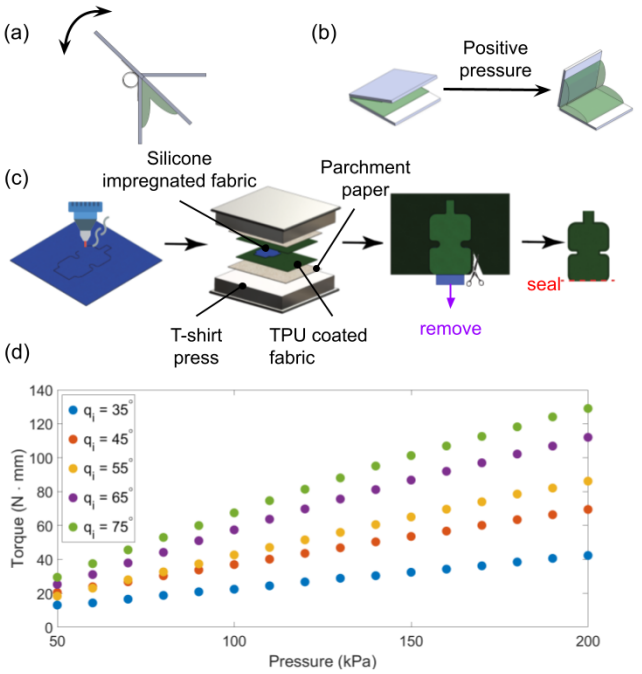

Fig. 3. **(a)** The pouch and antagonistic spring act together to move the legs of the device. **(b)** Operating principle of the pouch actuators: inflating one of these pouches moves the legs of the device. **(c)** The pouch manufacturing process. **(d)** Relationship between pouch pressure and joint torque at different joint angles.

From here, we can say that

$$J = J_v^{-1} J_q \tag{8}$$

and

$$J\dot{\overrightarrow{q}} = \overrightarrow{v}.$$

Eq.(6), Eq.(7), and Eq.(8) give us the Jacobian that we can use to iteratively solve forward kinematics, as originally presented by Nabat [30]. Let us define the current position of the end effector at time t as $\overrightarrow{p_t} = [x_t, y_t, z_t, \theta_t]^T$ and the position of the end effector at the previous time step, $t - \Delta t$, as $\overrightarrow{p_{t-\Delta t}} = [x_{t-\Delta t}, y_{t-\Delta t}, z_{t-\Delta t}, \theta_{t-\Delta t}]^T$. We then define the change in joint angle between time steps as, $\dot{\overrightarrow{q_t}} = \frac{\overrightarrow{q_t} - \overrightarrow{q_{t-\Delta t}}}{\Delta t}$, which allows us to write the following update rule for the iterative solution:

$$\overrightarrow{p_t} = \overrightarrow{p_{t-\Delta t}} + J\dot{\overrightarrow{q_t}}.$$

While the iterative solution is sufficient for most applications, one may want to solve the forward kinematics directly for a more accurate result. The direct solution to the forward kinematics is non-trivial and is similar to what was originally presented by Williams et al. [5].

C. Pneumatic Pouch Actuation and Fabrication

The device is actuated by four pneumatic pouches, which act against antagonistic springs, as depicted in Fig. 3(a). These pouches are 15 mm × 20 mm. When these pouches are not inflated, the springs exert torque on the device's legs, causing the tactor to rest just above the user's finger pad. Upon inflation of any of the four pouches, the corresponding leg rotates, moving the origami structure, and exerting force and torque on the user's finger pad by pushing the tactor against it. The way in which the inflation of these pouches imparts a torque on each leg is depicted in Fig. 3(b). These pouches rotate the joints from $q_i = 75°$ in the neutral position, to a maximum joint angle of $q_i = 35°$. This results in the maximum measured displacements shown in Table II. These measurements were taken with a camera tracking system (HX60 MicronTracker, ClaroNav) and align closely with the theoretical maximum displacements that can be calculated using the inverse kinematics described in Section III-B. The only direction where there is a notable discrepancy is in the θ direction, where friction between the 3D printed housing for the force sensor and Fourigami's frame causes a slight reduction in twist.

These pouches are manufactured by heat-pressing layers of thermoplastic polyurethane coated fabric with a mask that prevents the inside of the pouch from being sealed. Initially, a layer of silicone-impregnated fabric, designed to match the unsealed portion of the pouch with an added tail, is laser cut using a CO_2 laser cutter. This fabric, sandwiched between two layers of 40D TPU-coated ripstop nylon fabric, is sealed using a T-shirt press set at 360°F for 60 seconds. Subsequently, the silicone-impregnated fabric is removed by the tail. The pouch is then cut from the fabric and the bottom of the pouch is then sealed using an ultrasonic welder. This process is depicted in Fig. 3(c).

Once the pouch is made, a small piece of fishing wire is inserted to help air flow through both portions of the pouch. Finally, a small plastic tube is then pushed into the pouch's neck and secured in place using adhesives so that it can be easily connected to the pressure regulators (Loctite 401 and Riverruns Bonding and Welding UV Glue).

These pouches are then integrated into the origami structure as an added layer, as depicted in Fig. 4. When the device is folded together, the pouches are already in place. Throughout operation, the maximum pressure command sent to the pressure regulators never exceeds 200 kPa.

The plot shown in Fig. 3(c) shows the relationship between pressure and joint torque at different joint angles for pressures ranging from 50 kPa to 200 kPa. At 200 kPa the joint torques range from 42 N·mm to 129 N·mm, which highlights the primary motivation for using pneumatic pouches as opposed to DC motors. In addition to reducing the mass of the device at the fingertip by allowing the joint torques to be generated by off-board pressure regulators, the choice of pneumatic pouch actuation also produces greater maximum joint torques. For comparison, similar finger pad haptic devices [2], [5] use DC motors with stall torques of up to 15.4 N·mm and 29.9 N·mm, respectively. It should be noted that the use of off-board pressure regulators does mean that the device is not portable. Although this is acceptable for the VR and teleoperation applications Fourigami is designed for, as well as some AR tasks, such an actuation strategy would be much more difficult to implement in a device intended for the user to carry and travel with.

IEEE Transactions on Robotics (T-RO) paper, presented at ICRA 2026, Vienna, Austria. Cite as T-RO paper.

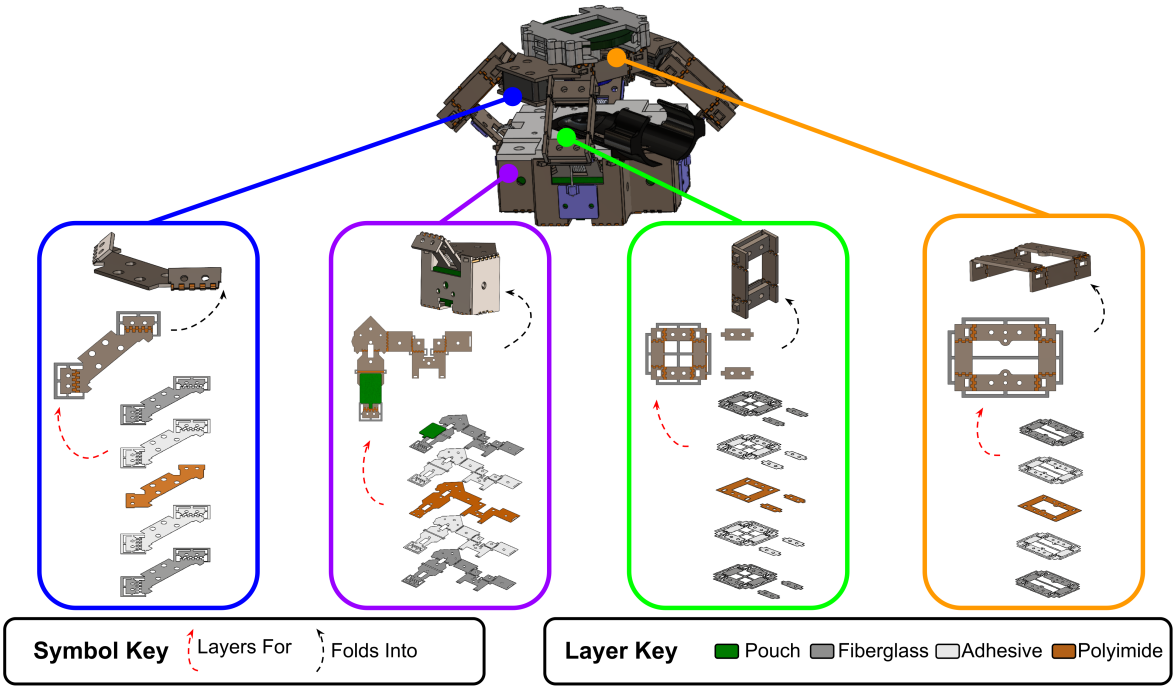

Fig. 4. Main origami components of the Fourigami device, their layers, what they fold into, and location on the device.

TABLE II
THEORETICAL AND MEASURED MAXIMUM TACTOR DISPLACEMENT

Direction	Theoretical Max Displacement	Measured Max Displacement
+x (mm)	5.6	5.6 ± 0.3
-x (mm)	5.6	5.6 ± 0.3
+y (mm)	5.4	5.5 ± 0.3
-y (mm)	5.4	5.5 ± 0.3
+z (mm)	7.4	7.2 ± 0.3
$+\theta$ (°)	24	20 ± 2.8
$-\theta$ (°)	24	21 ± 2.8

D. Origami Structure Fabrication

The origami structure of the device comprises four legs, four four-bar linkages, four pouches, four springs, and a top four-bar linkage enabling the twisting degree of freedom on the traveling plate. This top linkage is also where the force sensor and tactor are attached to the device.

All linkages within the origami structure are made from a polyimide and fiberglass laminate. Each fiberglass layer is cut from 10 mil fiberglass sheets on a UV Laser Cutter (DPSS Lasers Inc., Samurai UV Marking System) and the polyimide and adhesive layers are cut using a CO_2 laser cutter (PLS 6150 Laser Engraving System, Universal Laser Systems, Inc.). Polyimide layers are cut from a 5 mil sheet and adhesive layers are cut from a roll of heat- and pressure-activated adhesive (Pyralux LF0100R, Dupont). Once all layers are cut, they are then assembled as shown in Fig. 4 on a 3D printed jig and attached using a soldering iron. The laminate is then put on a heat press set to 300 PSI and 360 °F. The design incorporates gaps in the fiberglass to expose the polyimide, effectively creating hinges within the structure. These hinges are castellated to create more repeatable and localized bending of the joints [31]. In their flat state, each of these components has a bridge attached to them which holds the fiberglass in place during the heat pressing process and makes it so that the hinges cannot be bent. When parts are removed from the heat press, these bridges are cut first, before the components are folded into their final state, and the device is assembled. Figure 4 illustrates the layer-by-layer construction of the device and what these components are folded into.

Once the individual pieces are folded, they are screwed together to create the device depicted in Fig. 1.

IV. DEVICE CONTROL

A. Control Strategy

At the start of the control loop, a force command is sent to the device. In a VR or AR application, this force command is typically calculated using a "god-object" [32] or "finger-proxy" [33] algorithm. In both of these algorithms, the difference in position and orientation of the finger in the virtual environment and in real 3D space is measured in Fourigami's four degrees of freedom (x, y, z, and θ). This difference in pose is then scaled by a set of spring stiffnesses that represent the stiffness of the interaction and. Both the pose and spring stiffnesses are then used to compute the interaction forces. (In a robot teleoperation scenario, forces in the same four degrees of freedom would be measured or estimated by sensors on the robot manipulator, as has been done in other telerobotics research [34]–[36]. Those forces would then be sent as commands to the haptic device to provide direct force feedback.) Once the force command is calculated, the device uses the following control strategy: The force command is

IEEE Transactions on Robotics (T-RO) paper, presented at ICRA 2026, Vienna, Austria. Cite as T-RO paper.

sent to a proportional integral derivative (PID) controller, using filtered data derived from the force sensor embedded within the tactor. The output of the PID controller is subsequently added to the original reference command and further translated into a pressure command using the force-to-pressure mapping (F / P mapping) described in Section IV-B. Following this translation, the pressure command is filtered by an infinite impulse response (IIR) filter in order to reduce jitter and is then sent to the pressure regulators.

The pressure regulators have their own internal control loop, which is treated as a "black box" in our device control scheme. These pressures, in turn, inflate the pneumatic pouches on the device, enabling the tactor to exert forces against the user's finger. These forces are then read by the F/T sensor in the tactor, and this signal is again filtered by an IIR filter before it is fed back into the PID controller. This control strategy is depicted in Fig. 5 a. Throughout the control loop, IIR filters were used as they are computationally simple, did not induce any instabilities, and did not hinder tracking accuracy. However, other digital low-pass filters may also be adequate.

B. Force Mapping and Tracking Accuracy

The force sensor in the tactor is a capacitive 6-axis force / torque sensor that has a diameter of 21.3 mm, is 2 mm thick and weighs approximately 2 g [39]. The sensor is calibrated to 5 N, 2 N, and 15 N·mm in the normal, shear and torsional directions, respectively, while placed on top of a commercial force / torque sensor (Gamma SI-32, ATI) which we used as a reference. Sampling at 360 Hz, the sensor has an RMS error of 0.066 N, 0.076 N, and 0.6 mN·mm, in the normal, shear, and torsional directions, respectively.

The force-to-pressure mapping shown in Fig. 5 is used to translate the desired force command generated by the controller into a pressure command that is sent to the regulators. Through tests conducted on both a silicone phantom and on human fingers, we found that this mapping must change based on the mechanical properties of the surface that the tactor is in contact with. This means that each user must have their own mapping, which is measured before the wearer begins to use the device. We found that this mapping not only changes from person to person but also changes depending on how exactly the user wears the device because mechanical properties of the finger pad can also vary based on location.

Before testing the device on people, we began by attaching Fourigami to a silicone phantom with mechanical properties similar to those of a human finger. This phantom was used as a repeatable test setup for the trajectory tracking experiments discussed in this section and bandwidth and response time experiments discussed in Section V. Using known normal and shear stiffness properties of human finger pads as reference [22]–[24], we used Smooth On 00-30 silicone to make a phantom with similar mechanical properties using the established mechanical properties for that material [40]. Figure 5(a) shows the compressive force versus displacement relationship for the silicone phantom that was calculated using the uniaxial tension stress-strain relationship provided by Bergstrom et al. [37]. It also provides force vs. displacement measurements of two different fingers from Dzidek et al. [23] and Pawluk et al. [24]. The curve taken from Pawluk et al. is the instantaneous elastic response of the finger pad to loading, and the data from Dzidek et al. is from a finger pad tested at 45°. Figure 5(b) shows the shear force versus displacement relationship for the silicone phantom using the shear stress-strain relationship provided by Lohr et al. [38]. Although much work has been done to characterize the nonlinear force versus displacement relationship for the finger pad under compression, much less work has been done to characterize the finger pad in shear. However, Nakazawa et al. conducted some shear force versus displacement experiments on several fingers, where they modeled the finger as a linear elastic spring [22]. The range of stiffnesses they measured are shown as the blue region in Fig. 5(c).

In order to determine a force-to-pressure mapping for the silicone phantom, we conducted a series of experiments involving the application of 1000 sets of four random pressure commands, measuring the steady-state force read by the sensor in the tactor. Using half of this data, we used stepwise regression to fit second-order models with interactions to the training set. These models predict the four pressures based on the desired force output and had a test RMSE ranging from 7.1 to 10.0 kPa, depending on the pouch, along with adjusted R^2 values ranging from 0.978 to 0.992. This mapping was then used for experiments that demonstrate the device's bandwidth and transient response.

Although the mechanical properties of the silicone are similar to those of a human finger, the mechanical properties of human fingers vary substantially from person to person [21]–[23]. Consequently, we devised a shorter mapping experiment for each individual user before they use the device. This condensed mapping experiment fits a second-order model with interactions to 100 data points, which took five minutes to collect. We used it instead of the mapping that was developed for the silicone phantom. For the user who wore the device in the virtual reality demonstration, henceforth referred to as Person A, 200 data points were collected over a 10-minute period. The first 100 were used to derive their mapping and that mapping had a RMSE test ranging from 14.2 to 28.2 kPa, depending on the pouch, along with adjusted R^2 values ranging from 0.961 to 0.988.

In order to demonstrate the tracking accuracy of this control strategy, we applied a series of 0.5 Hz sinusoidal commands in each direction and measured the resulting force output. The results of this experiment are shown in Fig. 6. We first looked at the tracking accuracy of the device when it was affixed to the silicone and when worn by Person A. The time series data for this experiment are shown in Fig. 6(a). For the test on the silicone phantom, the root mean square tracking errors (RMSE) were 0.046 N, 0.036 N, 0.163 N, and 0.262 N·mm for F_x, F_y, F_z, and M_z respectively. Similarly, for the test on Person A, the RMSE were 0.047 N, 0.040 N, 0.170 N and 0.222 N·mm for F_x, F_y, F_z, and M_z respectively, indicating that the smaller data set used to find the mapping for an individual person is sufficient despite being 1/10 th the size of the dataset for the silicone mapping.

In order to assess whether this trajectory tracking accuracy

IEEE Transactions on Robotics (T-RO) paper, presented at ICRA 2026, Vienna, Austria. Cite as T-RO paper.

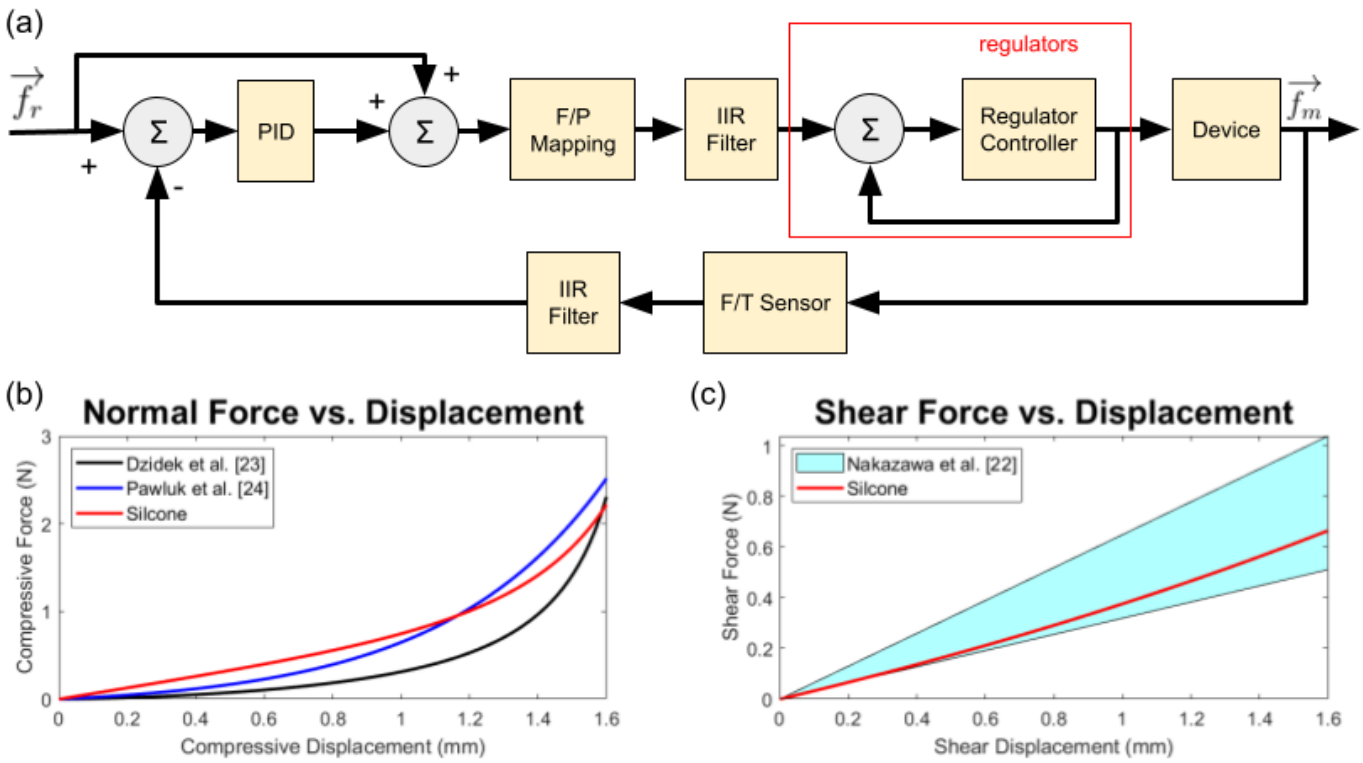

Fig. 5. **(a)** The device receives a reference command, $\overrightarrow{f_r}$, from the virtual environment that it feeds into a PID controller. The output of that controller is added to the reference and fed into an empirical mapping between force and pressure (depicted as F/P Mapping). Those pressure commands are fed into the pressure regulators that inflate the pouches in the device, and the resulting force vector $\overrightarrow{f_m}$, is read by the F / T sensor onboard and fed back into the control loop. Both pressure commands and F/T sensor readings are filtered by infinite impulse response (IIR) filters. **(b)** Force vs. displacement relationship for silicone phantom and actual finger stiffness measurements taken from [23], [24]. The stress-strain relationship for silicone under uniaxial compression was taken from [37] and used to calculate the silicone curve in this graph. **c)** This graph shows a range of shear stiffnesses taken from [22] and the shear force vs. displacement relationship for silicone. The silicone curve was calculated using the shear stress-strain relationship for silicone in shear from [38].

is sufficient, we look at the Just Noticeable Difference (JND), which is the minimum difference in force a person can perceive on their finger pad. Brothers et al. show that in the range of 0.7 to 4 N in the z direction, the JND ranges from roughly 0.2 to 0.4 N [41]. The fact that Fourigami's RMSE tracking error in the -z direction is below that range suggests that an individual would not be able to perceive the error in that direction. Although JND has not been measured explicitly in the shear direction, experiments conducted by Biggs and Srinivasan show that for a force applied in a shear direction to be perceived as equally intense to a force applied in the normal direction, it must be roughly 4 times the size of the normal force, indicating that human finger pads are less sensitive to shear forces than they are to normal forces [42]. Given that Fourigami's RMSEs in the shear directions are significantly smaller than in the normal direction, it is unlikely that an individual would be able to perceive the shear trajectory tracking error.

This suggests that Fourigami has suitable force trajectory tracking accuracy for applications where consistent and precise force rendering across different users is desired. An example of such an application would be training workers in an assembly task with delicate objects where force rendering information must be accurate enough to prevent users from breaking the objects. Another example is a psychophysical study where experimenters need to ensure the same force stimulus is applied to different users. Unfortunately, because the development of small F/T sensors for wearable haptic devices is recent, there is a lack of available data to compare the force tracking accuracy of Fourigami to that of other finger pad haptic devices.

Following this experiment, we investigated how changing the way the user wears the device affects tracking accuracy and how well the mappings for both silicone and another person, Person B, work when Person A is wearing the device. This data is summarized in Fig. 6(b). In both of these later experiments, the same set of sinusoidal commands as shown in Fig. 6(a) was used.

This data confirms that each individual user needs their own mapping. This can be clearly seen in the right most plot in Fig. 6(b) where the RMSE for trajectories tracked on Person A using the mapping for Person A is smaller than when Person A uses the silicone mapping or when Person B uses the mapping for Person A.

We also observed that the tracking accuracy for a single mapping changes based on how the user wears the device. This can be seen in the plot on the left in Fig. 6(b). For this experiment, Person A donned the device as they would normally. They then pushed their finger farther forward and then pulled their finger backward as shown in the graphic on Fig. 6(b). During this test, we observed that the mapping found for Person A who wore the device in the nominal position produced less accurate tracking when they moved their finger

IEEE Transactions on Robotics (T-RO) paper, presented at ICRA 2026, Vienna, Austria. Cite as T-RO paper.

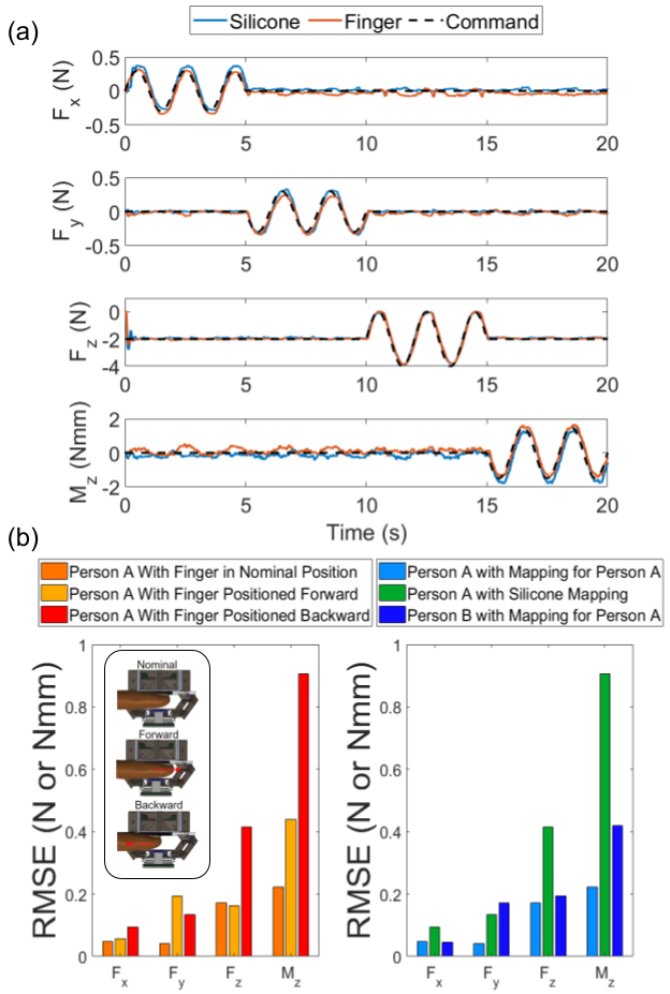

Fig. 6. **(a)** Time series data showing the tracking accuracy of the controller in two scenarios. First, when the device is attached to a piece of silicone and using the F/P mapping for that silicone, and second, when the device is worn by an individual, Person A, and the controller is using the mapping for Person A. **(b)** Root mean square tracking errors (RMSE) for a variety of conditions. All of these tests were performed using the same commands shown in (**a**). The graph on the left shows how the RMSE changes based on how Person A uses the device. All of these tests were performed using the mapping for person A. The graph on the right shows how the RMSE changes based on the mapping used. In this test, Person A is wearing the device in the nominal position and is using either their own mapping or the silicone mapping. For comparison, Person B also wears the device in the nominal position using the mapping for Person A.

to a different position. This is likely because the mechanical properties of the finger not only vary from person to person but also vary in different locations on the same person's finger pad as the tactor acts closer to or farther from the distal interphalangeal joint. As such, the force-to-pressure mapping for each user should be individualized to the user and how they have chosen to wear the device to have the most accurate force rendering. Fortunately, only five minutes of data is required to attain an accurate mapping for an individual user.

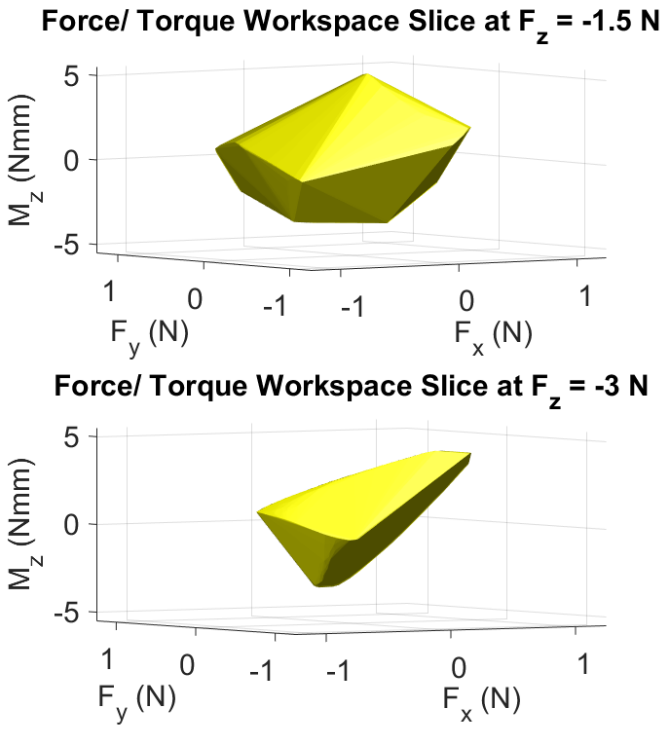

Fig. 7. Slices of the force workspace for Person A at two different normal forces. These plots were generated using the mapping discussed in Section IV-B and shows the maximum reachable force vectors that could be provided to Person A.

V. Device Performance

A. Force Output

When trying to assess the efficacy of a finger pad haptic device, the maximum force that the device can apply is a relevant metric because it limits the range of force vectors that can be rendered from a virtual environment or teleoperation scenario. Unfortunately, papers on previously developed finger pad haptic devices have not been able to provide this information because force sensors are usually too large to be incorporated into the device in a way that allows force applied to the finger pad to be measured directly. Instead, many of these papers provide the blocked force [2], [5], [6]. We have provided both the blocked force and the force applied to a human finger pad in Table III and in Table I which provides a comparison with other finger pad haptic devices. It is worth noting that the force and torque applied to the finger pad is significantly smaller than the blocked force measurements due to the finger pad's compliance. We also expect that the maximum force that can be applied to a finger pad would vary from person to person depending on the mechanical properties of their finger.

To perform the blocked force tests, we secured the device in its neutral position and rigidly affixed the tactor to a 6 axis F/T sensor (Nano 17 SI-50-0.5, ATI). Throughout this test, the device applied forces in each direction and the result was measured by the ATI F/T sensor. In order to measure the maximum force applied to a finger pad, an individual wore the

IEEE Transactions on Robotics (T-RO) paper, presented at ICRA 2026, Vienna, Austria. Cite as T-RO paper.

TABLE III
MAXIMUM FORCE APPLIED TO A HUMAN FINGER PAD AND MAXIMUM BLOCKED FORCE AT FOURIGAMI'S TACTOR

Direction	Force/Torque on Finger Pad	Blocked Force/Torque
+x	1.0 N	2.4 N
-x	-1.0 N	-2.2 N
+y	1.2 N	2.3 N
-y	-1.0 N	-2.0 N
-z	- 4.5 N	-5.6 N
$+\theta$	5.4 N·mm	11 N·mm
$-\theta$	-4.2 N·mm	-13 N·mm

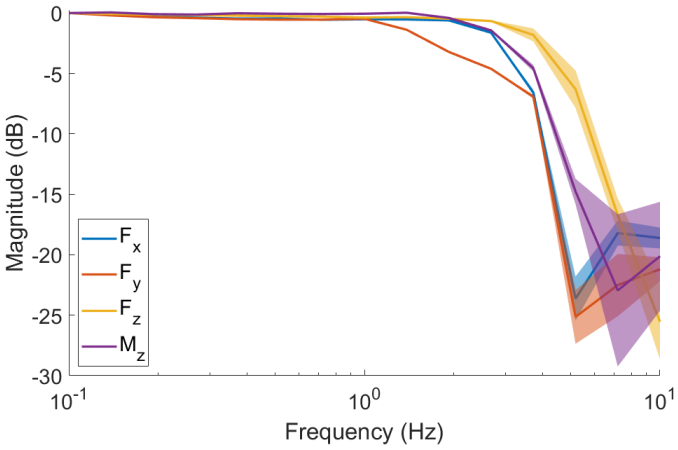

Fig. 8. Fourigami device Bode plot with 95% confidence intervals. The -3dB bandwidth with 95% confidence intervals is listed in Table IV.

TABLE IV
DEVICE BANDWIDTH IN EACH DIRECTION WITH 95% CONFIDENCE INTERVALS. THE CORRESPONDING BODE PLOT IS SHOWN IN FIG. 8

Direction	Bandwidth (Hz)
x	2.94 ± 0.04
y	2.08 ± 0.12
z	4.13 ± 0.27
θ	3.17 ± 0.09

device, forces were applied in each direction, and the resulting force and torque were measured by the integrated force sensor.

Using the force-to-pressure mapping discussed in Section IV-B, we can also define a force workspace. This workspace is a four-dimensional surface within which any force vector should be achievable. Much like the maximum forces we measured on a finger pad, this workspace is also person-dependent. Slices of the force workspace for Person A are shown in Fig. 7. From this graph, we can see that as we increase the commanded force F_z, the maximum reachable commands for F_x, F_y and M_z decrease. This can be observed by noting the change in force workspace size of different F_z commands.

B. Bandwidth and Transient Response

For the purpose of measuring the device's bandwidth across different directions, sinusoidal trajectories were sent to the device as reference commands, while the tactor was attached

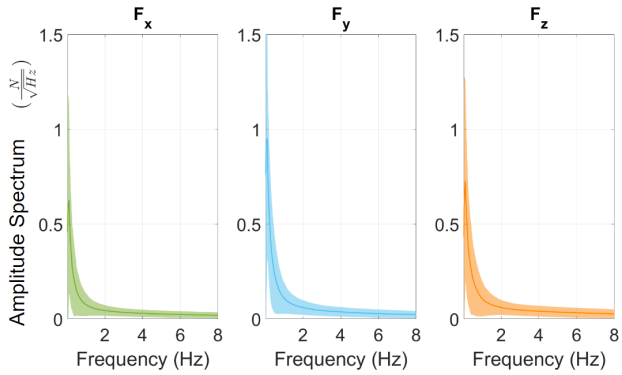

Fig. 9. ASD Plot made from data provided by a study conducted by Palmer et al [43] in which individuals were asked to pick up and move blocks in a virtual environment. This plot was made by taking data for a single participant in that study and shows the average ASD surrounded by a 1 standard deviation band.

to a piece of silicone with stiffness properties similar to those of a human finger. This is the same piece of silicone discussed Section IV-B.

When commanding sinusoidal trajectories that varied in the shear or twist directions, the force commanded on the z-axis was kept constant. In contrast, when a sinusoidal trajectory was applied in the z-direction, commands for shear forces and twist were set to 0 N and 0 N·mm, respectively. This is because when the device is worn, it must apply forces in the z-direction to the finger pad in order for shear forces and twist to be felt. These trajectories are similar to the ones shown in Fig. 6.

Sinusoids spanning frequencies from 0.1 to 10 Hz, lasting 15 periods, were commanded. Subsequently, the force outputs were measured using the force sensor in the tactor. The resulting Bode plots, detailing system responses, are depicted in Fig. 8. The -3 dB bandwidth for each direction is listed in Table IV along with 95% confidence intervals. While we primarily analyzed the tracking accuracy of the device for the 0.5 Hz signal discussed in Section IV-B, we did not observe a noticeable decline in tracking accuracy until the -3dB point.

Comparatively, the observed bandwidths in all directions are lower than those documented in similar finger pad haptic devices [2], [5], [6]. Despite this, we maintain the perspective that the bandwidth is adequate for VR applications.

We arrived at this conclusion by analyzing data derived from a study in which participants interacted with blocks using haptic feedback in a virtual environment [43]. In this study, users completed various tasks that involve picking up and manipulating blocks in virtual reality, which is very similar to the kinds of VR tasks for which we imagine Fourigami would be used. We took data from a single participant in this study who completed 50 trials of picking up and moving blocks in a virtual environment. From that data, we plotted an Amplitude Spectrum Density (ASD) plot of the forces calculated by the virtual environment in order to better understand the bandwidth of a device required to complete these sorts of tasks. This ASD plot, shown in Fig. 9, shows that the predominant portion of the normal and shear force commands operate below 2 Hz. This observation suggests that Fourigami should be able to render meaningful haptic feedback for comparable

IEEE Transactions on Robotics (T-RO) paper, presented at ICRA 2026, Vienna, Austria. Cite as T-RO paper.

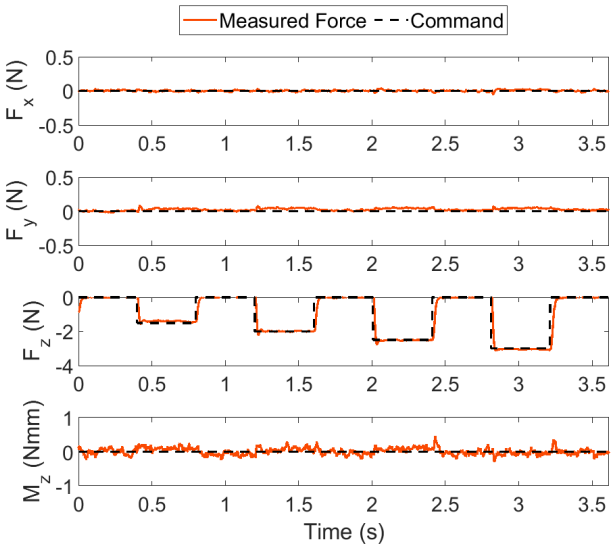

Fig. 10. Time series data showing the device tracking step inputs in the z direction when affixed to a piece of silicone. The corresponding rise and fall times for this experiment are shown in Table V.

TABLE V
RISE AND FALL TIMES FOR STEP INPUTS IN THE Z DIRECTION. THESE TIMES WERE TAKEN FROM THE PLOT SHOWN IN FIG. 10

	Rise Time (ms)	Fall Time (ms)
-1.5 N	34	69
-2 N	35	83
-2.5 N	47	83
-3 N	53	92

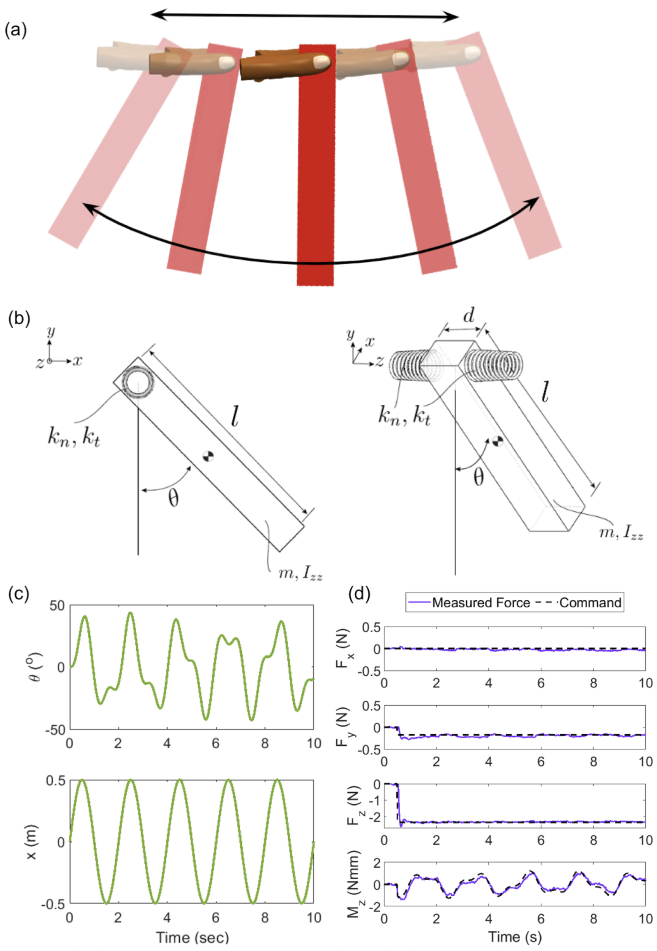

Fig. 11. **(a)** A visual representation of the demonstration scenario. This image was made from frames taken from a motion study conducted on this scenario shown in the *Object Interaction Trajectory Tracking* section of the supplementary video. **(b)** A diagram showing the physical parameters of the scenario. **(c)** plots of the set trajectory for x and the calculated trajectory for θ. **(d)** The commanded and measured forces rendered to a human finger pad during the demonstration.

VR scenarios and is also the reason we focused on the 0.5 Hz frequency when looking at trajectory tracking accuracy in Section IV-B.

In addition to looking at the device's bandwidth, we also investigated its transient response by looking at the rise and fall time for step inputs in the z-direction ranging from -1.5 N to -3 N. In this case, the rise time is the amount of time it takes the device to apply the corresponding force to the finger pad, while the fall time is the amount of time it takes to return to 0 N after having applied a step input. The time series data for this experiment are shown in Fig. 10 and the corresponding rise and fall times are summarized in Table V. The rise times range from 34 to 53 ms and the fall times from 69 to 92 ms, indicating that the device can provide haptic feedback without noticeable delay in VR applications [44].

VI. DEMONSTRATION

While Fourigami could be used for VR, AR, and teleoperation applications, here we focus on the VR application. In order to demonstrate Fourigami's ability to track force trajectories that could be generated by VR interactions, we modeled a realistic VR scenario, calculated the trajectory, and demonstrated Fourigami tracking that trajectory on a human finger pad. The scenario we modeled was a person grasping a rectangular object between their index finger and thumb and moving their hand side to side so that the object oscillates between their fingers. This motion is depicted in Fig. 11(a) and is shown in the motion study video provided in the supplementary materials.

Most standard haptics rendering algorithms model the contact forces between the finger and an object as a spring with stiffness in the normal and shear directions [32], [33], [45]. While this is an inaccurate model that does not account for the nonlinear force versus displacement relationship of the human finger pad, these rendering algorithms have been shown to provide sufficiently realistic haptic interaction calculations for a wide variety of VR user studies [2], [4], [8], [43], [46], demonstrations [5], [47], and training simulators [48]–[50], and are commonplace for this application [51]. Here, we use the same strategy and also give that spring a torsional stiffness. This spring has a stiffness in the normal direction of k_n and a torsional stiffness of k_t. The object also has length l, mass m, and a moment of inertia about its center of $I_{zz} = 1/12\, m(l^2 + d^2)$. This is depicted in Fig. 11(b).

In this scenario, the user moves the object in the x direction with such that $x = A\sin(2\pi f t)$ as shown in Fig. 11(b). We then used Lagrangian mechanics to get the equation of motion

IEEE Transactions on Robotics (T-RO) paper, presented at ICRA 2026, Vienna, Austria. Cite as T-RO paper.

TABLE VI
PARAMETERS USED TO CALCULATE FORCES RENDERED TO THE FINGER PAD

Parameter	Value
m	35 g
l	0.2 m
d	0.05m
k_n	0.38 N/mm
k_t	2.1 N·mm/rad
A	0.5 m
f	0.5 Hz
g	9.8 m/s^2
z_{comp}	5.3 mm

for the object

$$\frac{1}{2}m\ddot{x}l\cos\theta + (I_{zz} + \frac{1}{2}ml^2)\ddot{\theta} + 2k_t\theta + \frac{1}{2}mgl\sin\theta = 0 \quad (9)$$

and modeled the forces rendered to the index finger pad as

$$\begin{bmatrix} F_x \\ F_y \\ F_z \\ M_z \end{bmatrix} = \begin{bmatrix} 0 \\ -\frac{mg}{2} \\ -k_n z_{\text{comp}} \\ -k_t\theta \end{bmatrix} \quad (10)$$

.

We then numerically solved Eq.(9) for θ, and used that to calculate M_z. The values used in this calculation are given in Table VI.

We give the object a stiffness of 0.3 N/mm as objects for similar VR haptic interactions have ranged from 0.1 to 0.5 N/mm [2], [5], and we give the finger pad a normal stiffness of 1.58 N/mm, which matches values found in the literature and used in similar VR haptics models [2], [5], [33]. k_t is the combined stiffness of the finger pad and the object in series. Finally, we give the finger pad a torsional stiffness of 2.1 N·mm/rad based on the measurements carried out by Escoffier et al. [52]. In order to use these values with our simplified torsion spring model for haptic rendering, we only used the instantaneous elastic response derived in this work. The value of z_{comp} was chosen so that F_z would be high enough to prevent the object from slipping. We checked this by looking at experiments conducted by Barbagli et al.[33] in which people were asked to press their fingers against a polyurethane pad attached to a motor. The motor then applied a torque to try to rotate the pad, and the torque at which the pad started to rotate and slip on the finger pad was recorded along with how hard the person was pressing against the pad. Giving the virtual object similar frictional properties to the polyurethane pad used in this study, the values of M_z are well below the amount of torque required to cause the object to slip subject to the applied F_z.

In some VR scenarios, slip is ignored entirely so that the haptic rendering can be simplified, so for our demonstration we chose to focus on a case where the object does not slip and implement a similar haptic rendering algorithm to the one used by Williams et al. [5]. However, when slip is taken into account, the algorithm is quite similar. In this case, k_t is chosen to represent the frictional properties of the object rather than the torsional stiffness of the finger pad, and M_z only changes when the object slips [2], [33]. Although the values of M_z are likely to be quite similar for the case where the object is slipping, we acknowledge this choice as a limitation of the demonstration and leave validation of rendering cases where objects slip in the user's fingers to future work.

Once the desired force trajectory was calculated, again assuming that the object does not slip, we then commanded Fourigami to track that trajectory on a human finger pad. Fig. 11d shows the desired trajectory and force measured by Fourigami's internal F/T sensor. The device had a root mean squared tracking error of 0.03 N in F_x, 0.04 N in F_y, 0.17 N in F_z, and 0.31 N·mm in M_z. The tracking error in F_z is also below the threshold for measured JND on the finger pad, as it was in Section IV-B, which further demonstrates Fourigami's ability to accurately track force trajectories for VR applications.

VII. CONCLUSION

We designed and fabricated a lightweight, 4-DoF, wearable haptic device for the finger pad, and demonstrated that it is capable of rendering compelling forces for interactions within virtual environments. In Fourigami's design, we showed how pneumatic pouches can be integrated into origami manufacturing techniques as a layer in the device's structure, allowing the actuators to be fully integrated into the device as it is folded together. Our characterization and demonstrations with the device show its potential for practical applications such as pick and place and assembly training tasks in VR and AR.

The authors acknowledge that while Section VI does demonstrate Fourigami tracking a trajectory that could be generated through interacting with objects in a virtual environment, further engineering work would need to be completed in order to integrate finger tracking and connect it to a virtual environment as in [2], [5], [43]. In this demonstration, we also only showed the case where the object does not slip. While the haptic rendering algorithms commonly used for slip are quite similar to the non-slip case we demonstrated in this work, we would also need to conduct VR demonstrations with slipping objects to confirm Fourigami can be used for this case. Furthermore, to use this device for a telerobotics application, communications between a sensorized manipulator and Fourigami would need to be established in order to render haptic feedback to the user. It is worth noting that while Fourigami is light-weight, it is not small enough that one of these devices could be worn on each finger. This limits the kinds of tasks Fourigami could be used for to tasks like discerning the stiffness of objects with a single finger or using the finger and thumb to manipulate objects. For example, Fourigami could be used in an assembly training task where someone uses their thumb and index finger to grasp, move, and assemble components, but it could not be used in a more complex assembly task that requires the use of the entire hand.

Looking ahead, we envision using this device to explore the impact of the twisting degree of freedom on user interactions with virtual objects and would like to further investigate different control strategies that are either less sensitive to different finger stiffnesses or require less data to provide an accurate force-to-pressure mapping.

IEEE Transactions on Robotics (T-RO) paper, presented at ICRA 2026, Vienna, Austria. Cite as T-RO paper.

ACKNOWLEDGMENT

The authors thank Dr. Sophia Williams for her guidance throughout this project and Anu Solola for helping to manufacture and test preliminary Fourigami prototypes.

REFERENCES

[1] D. Leonardis, M. Solazzi, I. Bortone, and A. Frisoli, "A 3-RSR Haptic Wearable Device for Rendering Fingertip Contact Forces," *IEEE Transactions on Haptics*, vol. 10, no. 3, pp. 305–316, 2017.

[2] S. B. Schorr and A. M. Okamura, "Three-dimensional skin deformation as force substitution: Wearable device design and performance during haptic exploration of virtual environments," *IEEE Transactions on Haptics*, vol. 10, no. 3, pp. 418–430, Jul 2017.

[3] R. V. Patel, S. F. Atashzar, and M. Tavakoli, "Haptic feedback and force-based teleoperation in surgical robotics," *Proceedings of the IEEE*, vol. 110, no. 7, pp. 1012–1027, 2022.

[4] J. M. Suchoski, A. Barron, C. Wu, Z. F. Quek, S. Keller, and A. M. Okamura, "Comparison of kinesthetic and skin deformation feedback for mass rendering," *Proceedings - IEEE International Conference on Robotics and Automation*, vol. 2016-June, pp. 4030–4035, 2016.

[5] S. R. Williams, J. M. Suchoski, Z. Chua, and A. M. Okamura, "A 4-Degree-of-Freedom Parallel Origami Haptic Device for Normal, Shear, and Torsion Feedback," *IEEE Robotics and Automation Letters*, vol. 7, no. 2, pp. 3310–3317, 2022.

[6] Z. Zhakypov and A. M. Okamura, "Fingerprint: A 3-d printed soft monolithic 4-degree-of-freedom fingertip haptic device with embedded actuation," in *IEEE 5th International Conference on Soft Robotics*, 2022, pp. 938–944.

[7] F. H. Giraud, S. Joshi, and J. Paik, "Haptigami: A Fingertip Haptic Interface with Vibrotactile and 3-DoF Cutaneous Force Feedback," *IEEE Transactions on Haptics*, vol. 15, no. 1, pp. 131–141, 2022.

[8] A. Girard, M. Marchal, F. Gosselin, A. Chabrier, F. Louveau, and A. Lécuyer, "HapTip: Displaying Haptic Shear Forces at the Fingertips for Multi-Finger Interaction in Virtual Environments," *Frontiers in ICT*, vol. 3, pp. 1–15, 2016.

[9] M. Solazzi, A. Frisoli, and M. Bergamasco, "Design of a novel finger haptic interface for contact and orientation display," *2010 IEEE Haptics Symposium, HAPTICS 2010*, pp. 129–132, 2010.

[10] D. Prattichizzo, F. Chinello, C. Pacchierotti, and M. Malvezzi, "Towards wearability in fingertip haptics: A 3-DoF wearable device for cutaneous force feedback," *IEEE Transactions on Haptics*, vol. 6, no. 4, pp. 506–516, 2013.

[11] Y. Ma, T. Xie, P. Zhang, H. Kim, and S. Je, "AirPush: A Pneumatic Wearable Haptic Device Providing Multi-Dimensional Force Feedback on a Fingertip," *Conference on Human Factors in Computing Systems - Proceedings*, 2024.

[12] E. M. Young and K. J. Kuchenbecker, "Implementation of a 6-DOF Parallel Continuum Manipulator for Delivering Fingertip Tactile Cues," *IEEE Transactions on Haptics*, vol. 12, no. 3, pp. 295–306, 2019.

[13] A. Bicchi, J. K. Salisbury, and D. L. Brock, "Experimental evaluation of friction characteristics with an articulated robotic hand," *Lecture Notes in Control and Information Sciences*, vol. 190, pp. 153–167, 1993.

[14] J. K. Salisbury and B. Roth, "Kinematic and force analysis of articulated mechanical hands," *Journal of Mechanical Design, Transactions of the ASME*, vol. 105, no. 1, pp. 34–41, 1983.

[15] Z. Zhakypov, M. Mete, J. Fiorentino, and J. Paik, "Programmable fluidic networks design for robotic origami sequential self-folding," in *RoboSoft 2019 - 2019 IEEE International Conference on Soft Robotics*. Institute of Electrical and Electronics Engineers Inc., May 2019, pp. 814–820.

[16] C. Pacchierotti, S. Sinclair, M. Solazzi, A. Frisoli, V. Hayward, and D. Prattichizzo, "Wearable haptic systems for the fingertip and the hand: Taxonomy, review, and perspectives," *IEEE Transactions on Haptics*, vol. 10, no. 4, pp. 580–600, 2017.

[17] A. Adilkhanov, M. Rubagotti, and Z. Kappassov, "Haptic Devices: Wearability-Based Taxonomy and Literature Review," *IEEE Access*, vol. 10, no. September, pp. 91 923–91 947, 2022.

[18] K. Iiyoshi, J. H. Lee, A. S. Dalaq, S. Khazaaleh, M. F. Daqaq, G. Korres, and M. Eid, "Origami-Inspired Haptics: A Literature Review," *IEEE Access*, vol. 12, pp. 33 309–33 327, 2024.

[19] S. Mintchev, M. Salerno, A. Cherpillod, S. Scaduto, and J. Paik, "A portable three-degrees-of-freedom force feedback origami robot for human–robot interactions," *Nature Machine Intelligence 2019 1:12*, vol. 1, no. 12, pp. 584–593, Dec 2019. [Online]. Available: https://www.nature.com/articles/s42256-019-0125-1

[20] H.-Y. Han and S. Kawamura, "Analysis of stiffness of human fingertip and comparison with artificial fingers," in *1999 IEEE International Conference on Systems, Man, and Cybernetics (Cat. No.99CH37028)*, vol. 2, 1999, pp. 800–805.

[21] C. Oprişan, V. Cârlescu, A. Barnea, G. Prisacaru, D. N. Olaru, and G. Plesu, "Experimental determination of the young's modulus for the fingers with application in prehension systems for small cylindrical objects," *IOP Conference Series: Materials Science and Engineering*, vol. 147, no. 1, p. 012058, 2016.

[22] H. I. N Nakazawa, R Ikeura, "Characteristics of human fingertips in the shearing direction," *Biological Cybernetics*, vol. 82, no. 3, pp. 207–214, 2000.

[23] B. M. Dzidek, M. J. Adams, J. W. Andrews, Z. Zhang, and S. A. Johnson, "Contact mechanics of the human finger pad under compressive loads," *Journal of the Royal Society Interface*, vol. 14, no. 127, 2017.

[24] D. Pawluk and R. Howe, "Dynamic lumped element response of the human fingerpad," *Journal of Biomechanical Engineering*, vol. 121, pp. 178–183, 1999.

[25] B. Li and G. J. Gerling, "Individual differences impacting skin deformation and tactile discrimination with compliant elastic surfaces," in *2021 IEEE World Haptics Conference*, 2021, pp. 721–726.

[26] Y. Kamikawa, N. Enayati, and A. M. Okamura, "Magnified force sensory substitution for telemanipulation via force-controlled skin deformation," in *2018 IEEE International Conference on Robotics and Automation (ICRA)*, 2018, pp. 4142–4148.

[27] Z. F. Quek, S. B. Schorr, I. Nisky, A. M. Okamura, and W. R. Provancher, "Sensory augmentation of stiffness using fingerpad skin stretch," in *2013 World Haptics Conference (WHC)*, 2013, pp. 467–472.

[28] Z. F. Quek, S. B. Schorr, I. Nisky, W. R. Provancher, and A. M. Okamura, "Sensory substitution using 3-degree-of-freedom tangential and normal skin deformation feedback," in *2014 IEEE Haptics Symposium (HAPTICS)*, 2014, pp. 27–33.

[29] F. Pierrot, V. Nabat, O. Company, S. Krut, and P. Poignet, "Optimal design of a 4-dof parallel manipulator: From academia to industry," *IEEE Transactions on Robotics*, vol. 25, no. 2, pp. 213–224, 2009.

[30] V. Nabat, "Robots parallèles à nacelle articulée du concept à la solution industrielle pour le pick-and place," Ph.D. dissertation, University of Montpellier, 2007.

[31] N. Doshi, B. Goldberg, R. Sahai, N. Jafferis, D. Aukes, R. J. Wood, and J. A. Paulson, "Model driven design for flexure-based microrobots," in *2015 IEEE/RSJ International Conference on Intelligent Robots and Systems (IROS)*, 2015, pp. 4119–4126.

[32] C. Zilles and J. Salisbury, "A constraint-based god-object method for haptic display," in *Proceedings 1995 IEEE/RSJ International Conference on Intelligent Robots and Systems. Human Robot Interaction and Cooperative Robots*, vol. 3, 1995, pp. 146–151.

[33] F. Barbagli, A. Frisoli, K. Salisbury, and M. Bergamasco, "Simulating human fingers: a soft finger proxy model and algorithm," in *12th International Symposium on Haptic Interfaces for Virtual Environment and Teleoperator Systems*, 2004, pp. 9–17.

[34] T. Hirabayashi, J. Akizono, T. Yamamoto, H. Sakai, and H. Yano, "Teleoperation of construction machines with haptic information for underwater applications," *Automation in Construction*, vol. 15, no. 5, pp. 563–570, 2006, 21st International Symposium on Automation and Robotics in Construction. [Online]. Available: https://www.sciencedirect.com/science/article/pii/S0926580505001007

[35] K. J. Kuchenbecker, *Haptics and Haptic Interfaces*. Springer Berlin Heidelberg, 2018, pp. 1–9.

[36] R. V. Patel, S. F. Atashzar, and M. Tavakoli, "Haptic feedback and force-based teleoperation in surgical robotics," *Proceedings of the IEEE*, vol. 110, no. 7, pp. 1012–1027, 2022.

[37] J. Bergström, *Elasticity/Hyperelasticity*, 2015.

[38] M. J. Lohr, G. P. Sugerman, S. Kakaletsis, E. Lejeune, and M. K. Rausch, "An introduction to the Ogden model in biomechanics: Benefits, implementation tools and limitations," *Philosophical Transactions of the Royal Society A: Mathematical, Physical and Engineering Sciences*, vol. 380, no. 2234, 2022.

[39] H. Choi, J. E. Low, T. M. Huh, G. A. Uribe, S. Hong, K. A. W. Hoffman, J. Di, T. G. Chen, A. A. Stanley, and M. R. Cutkosky, "Coinft: A coin-sized, capacitive 6-axis force torque sensor for robotic applications," 2025. [Online]. Available: https://arxiv.org/abs/2503.19225

[40] L. Marechal, P. Balland, L. Lindenroth, F. Petrou, C. Kontovounisios, and F. Bello, "Toward a Common Framework and Database of Materials for Soft Robotics," *Soft Robotics*, vol. 8, no. 3, pp. 284–297, 2021.

[41] T. Brothers and M. Hollins, "Two sensory channels mediate perception of fingertip force," *Perception*, vol. 43, no. 10, pp. 1071–1082, 2014.

[42] J. Biggs and M. Srinivasan, "Tangential versus normal displacements of skin: relative effectiveness for producing tactile sensations," in *Proceedings 10th Symposium on Haptic Interfaces for Virtual Environment and Teleoperator Systems. HAPTICS 2002*, 2002, pp. 121–128.

[43] J. E. Palmer, M. Sarac, A. A. Garza, and A. M. Okamura, "Haptic feedback relocation from the fingertips to the wrist for two-finger manipulation in virtual reality," *2022 IEEE/RSJ International Conference on Intelligent Robots and Systems (IROS)*, pp. 628–633, 2022.

[44] J. M. Silva, M. Orozco, J. Cha, A. El Saddik, and E. M. Petriu, "Human perception of haptic-to-video and haptic-to-audio skew in multimedia applications," *ACM Transactions on Multimedia Computing, Communications and Applications*, vol. 9, no. 2, pp. 1–16, 2013.

[45] K. Salisbury, D. Brock, T. Massie, N. Swarup, and C. Zilles, "Haptic rendering: programming touch interaction with virtual objects," in *Proceedings of the 1995 Symposium on Interactive 3D Graphics*. New York, NY, USA: Association for Computing Machinery, 1995, p. 123–130.

[46] J. Suchoski, S. Martinez, and A. M. Okamura, "Scaling inertial forces to alter weight perception in virtual reality," in *IEEE International Conference on Robotics and Automation*, 2018, pp. 484–489. [Online]. Available: https://doi.org/10.1109/ICRA.2018.8462874

[47] I. Choi, E. Ofek, H. Benko, M. Sinclair, and C. Holz, "CLAW: A multifunctional handheld haptic controller for grasping, touching, and triggering in virtual reality," *Conference on Human Factors in Computing Systems - Proceedings*, vol. 2018-April, pp. 1–13, 2018.

[48] P. Abinaya and M. Manivannan, "Haptic based fundamentals of laparoscopic surgery simulation for training with objective assessments," *Frontiers in Robotics and AI*, vol. 11, no. May, pp. 1–21, 2024.

[49] J. Hergenhan, J. Rutschke, M. Uhl, S. E. Navarro, B. Hein, and H. Worn, "A haptic display for tactile and kinesthetic feedback in a chai 3d palpation training scenario," in *2015 IEEE International Conference on Robotics and Biomimetics (ROBIO)*, 2015, pp. 291–296.

[50] S. Valmiki and K. Rajamani, "Fabric paint environment using 3D haptics for vocational training," in *International Conference on Signal and Imagie Processing*, 2013, pp. 511–522.

[51] D. WANG, Y. GUO, S. LIU, Y. ZHANG, W. XU, and J. XIAO, "Haptic display for virtual reality: progress and challenges," *Virtual Reality and Intelligent Hardware*, vol. 1, no. 2, pp. 136–162, 2019. [Online]. Available: https://doi.org/10.3724/SP.J.2096-5796.2019.0008

[52] C. Escoffier, J. de Rigal, A. Rochefort, R. Vasselet, J. L. Lévêque, and P. G. Agache, "Age-related mechanical properties of human skin: an in vivo study," *Journal of Investigative Dermatology*, vol. 93, no. 3, pp. 353–357, 1989.

Crystal E. Winston (Member, IEEE) received the B.S. degree in mechanical engineering in 2019 from the Massachusetts Institute of Technology, Boston, MA, the MPhil degree in aerospace engineering in 2021 from Imperial College London, London, UK, and the Ph.D. degree in mechanical engineering in 2024 from Stanford University, Stanford, CA. Their research interests include haptics, origami robot design, and soft robotics.

Hojung Choi (Member, IEEE) received the B.S. degree in mechanical engineering and business administration in 2018 from the Ulsan National Institute of Science and Technology (UNIST), Ulsan, South Korea, the M.S. degree in mechanical engineering in 2020 from Stanford University, Stanford, CA, and the Ph.D. degree in mechanical engineering in 2024 from Stanford University, Stanford CA. His research interests include multimodal robot learning, tactile sensing, and manipulation.

Rianna Jitosho (Member, IEEE) received the B.S. degree in mechanical engineering in 2019 from the Massachusetts Institute of Technology, Boston, MA, and the M.S. degree in mechanical engineering in 2021 from Stanford University, Stanford, CA, and the Ph.D. degree in mechanical engineering in 2025 from Stanford University, Stanford CA. Her research interests include motion planning, controls, and soft robotics.

Zhenishbek Zhakypov received the Ph.D. degree in Robotics from the Swiss Federal Institute of Technology in Lausanne (EPFL). He is a former postdoctoral researcher in the Department of Mechanical Engineering at Stanford University. His research interests include the design, fabrication, and control methods for origami robots and haptic devices.

Jasmin E. Palmer (Member, IEEE) received the B.S. degree in mechanical engineering in 2019 from the Massachusetts Institute of Technology, Boston, MA, the M.S. degree in mechanical engineering in 2021 from Stanford University, Stanford, CA, and the Ph.D. degree in mechanical engineering in 2025 from Stanford University, Stanford, CA. Jasmin's research interests include human-computer interaction and haptics, virtual environments, and wearable devices.

Mark R. Cutkosky (Fellow, IEEE) received the Ph.D. degree in mechanical engineering from Carnegie Mellon University, Pittsburgh, PA, USA, in 1985. He is the Fletcher Jones Professor of Mechanical Engineering with Stanford University, Stanford, CA, USA. His research interests include bioinspired robots, haptics, and rapid prototyping processes. He is a Fellow of the ASME.

Allison M. Okamura (Fellow, IEEE) received the B.S. degree from the University of California Berkeley in 1994, and the M.S. and Ph.D. degrees from Stanford University, Stanford CA, in 1996 and 2000, respectively, all in mechanical engineering. She is currently the Richard W. Weiland Professor in the School of Engineering and Professor of Mechanical Engineering at Stanford University, Stanford, CA. Her research interests include haptics, teleoperation, medical robotics, virtual environments and simulation, neuromechanics and rehabilitation, prosthetics and engineering education.